AGU PUBLICATIONS

JGR

Journal of Geophysical Research: Atmospheres

RESEARCH ARTICLE
10.1002/2016JD025309

Key Points:
- Characterization of radiation interactions of clouds embedded in biomass burning smoke
- Multiangular airborne measurements of aerosol/clouds from a 3-D perspective
- Three-dimensional Monte Carlo radiative transfer simulations of aerosol/clouds and their interactions

Supporting Information:
- Supporting Information S1

Correspondence to:
R. Gautam,
rgautam@iitb.ac.in

Citation:
Gautam, R., C. K. Gatebe, M. K. Singh, T. Várnai, and R. Poudyal (2016), Radiative characteristics of clouds embedded in smoke derived from airborne multi-angular measurements, *J. Geophys. Res. Atmos.*, *121*, doi:10.1002/2016JD025309.

Received 2 MAY 2016
Accepted 16 JUL 2016
Accepted article online 21 JUL 2016

Radiative characteristics of clouds embedded in smoke derived from airborne multiangular measurements

Ritesh Gautam[1,2], Charles K. Gatebe[3,4], Manoj K. Singh[1], Tamás Várnai[4,5], and Rajesh Poudyal[6]

[1]Centre of Studies in Resources Engineering, Indian Institute of Technology Bombay, Mumbai, India, [2]Interdisciplinary Program in Climate Studies, Indian Institute of Technology Bombay, Mumbai, India, [3]Universities Space Research Association, Columbia, Maryland, USA, [4]NASA Goddard Space Flight Center, Greenbelt, Maryland, USA, [5]JCET, University of Maryland, Baltimore County, Baltimore, Maryland, USA, [6]Science Systems and Applications Inc., Lanham, Maryland, USA

Abstract Clouds in the presence of absorbing aerosols result in their apparent darkening, observed at the top of atmosphere (TOA), which is associated with the radiative effects of aerosol absorption. Owing to the large radiative effect and potential impacts on regional climate, above-cloud aerosols have recently been characterized in multiple satellite-based studies. While satellite data are particularly useful in showing the radiative impact of above-cloud aerosols at the TOA, recent literature indicates large uncertainties in satellite retrievals of above-cloud aerosol optical depth (AOD) and single scattering albedo (SSA), which are among the most important parameters in the assessment of associated radiative effects. In this study, we analyze radiative characteristics of clouds in the presence of wildfire smoke using airborne data primarily from NASA's Cloud Absorption Radiometer, collected during the Arctic Research of the Composition of the Troposphere from Aircraft and Satellites campaign in Canada during the 2008 summer season. We found a strong positive reflectance (R) gradient in the UV-visible (VIS)-near infrared (NIR) spectrum for clouds embedded in dense smoke, as opposed to an (expected) negative gradient for cloud-free smoke and a flat spectrum for smoke-free cloud cover. Several cases of clouds embedded in thick smoke were found, when the aircraft made circular/spiral measurements, which not only allowed the complete characterization of angular distribution of smoke scattering but also provided the vertical distribution of smoke and clouds (within 0.5–5 km). Specifically, the largest darkening by smoke was found in the UV/VIS, with $R_{0.34\mu m}$ reducing to 0.2 (or 20%), in contrast to 0.8 at NIR wavelengths (e.g., 1.27 μm). The observed darkening is associated with large AODs (0.5–3.0) and moderately low SSA (0.85–0.93 at 0.53 μm), resulting in a significantly large instantaneous aerosol forcing efficiency of $254 \pm 47\ W\ m^{-2}\ \tau^{-1}$. Our observations of smoke-cloud radiative interactions were found to be physically consistent with theoretical plane-parallel 1-D and Monte Carlo 3-D radiative transfer calculations, capturing the observed gradient across UV-VIS-NIR. Results from this study offer insights into aerosol-cloud radiative interactions and may help in better constraining satellite retrieval algorithms.

1. Introduction

The presence of partially absorbing aerosols (e.g., smoke and dust) above bright surfaces (e.g., clouds and snow) causes an apparent darkening of the underlying surface as observed at the top of atmosphere (TOA). The apparent darkening is associated with the aerosol-induced solar absorption above bright surfaces, and reduced scattered radiation at TOA. Darkening implies a warming effect of absorbing aerosols above clouds, which is in contrast to the cooling effect of aerosols above dark surfaces such as vegetation cover and ocean. Significant radiative impacts of clouds in the presence of absorbing aerosols have been observed over several regions including the persistent stratocumulus and stratiform cloud decks in southeast Atlantic regions [*Chand et al*., 2009; *de Graaf et al*., 2012; *Meyer et al*., 2013; *Zhang et al*., 2014; *Feng and Christopher*, 2015] and Southeast Asia [*Hsu et al*., 2003], respectively, as well as marine stratocumulus clouds off the coast of California [*Sorooshian et al*., 2007].

The marine stratocumulus layer in the southeast Atlantic, off the coast of Namibia, is often subjected to smoke plumes advected over cloud decks during the cold dry fire burning season (August–September) in southern Africa. Using satellite measurements from Polarization and Directionality of Earth Reflectances (POLDER) and Scanning Imaging Absorption Spectrometer for Atmospheric Chartography (SCIAMACHY), *Peers et al*. [2015] and *de Graaf et al*. [2012] estimated large monthly averaged aerosol-above-cloud forcing of $23\ W\ m^{-2}$–$33.5\ W\ m^{-2}$, with an order of magnitude larger forcing (exceeding 220 Wm^{-2}) during episodic events of high aerosol optical depth (AOD) and low single scattering albedo (SSA), suggesting enhanced

aerosol absorption. From a TOA perspective, these satellite imager-based studies have focused on the above-cloud radiative impact of aerosol absorption. The regional warming influence of aerosol absorption above clouds has also been studied in aerosol-cloud interactions using semidirect and thermodynamic pathways, showing changes in cloud liquid water path, cloud cover, and lower tropospheric stability [*Johnson et al.*, 2004; *Wilcox*, 2010, 2012; *Adebiyi et al*., 2015].

Owing to their large positive (warming) radiative effect and potential impacts on clouds and regional climate, co-occurring clouds and aerosols have recently been characterized in multiple satellite retrieval algorithms focused on deriving the above-cloud AOD and SSA information. *Waquet et al*. [2009] and *Peers et al*. [2015] used polarization measurements from POLDER/PARASOL to retrieve AOD and SSA for aerosols above marine stratocumulus clouds in the southeast Atlantic. Using UV reflectance measurements from the Ozone Monitoring Instrument, and VIS-NIR from the Moderate Resolution Imaging Spectroradiometer (MODIS), *Torres et al*. [2012], *Jethva et al*. [2013], *Meyer et al*. [2015], and *Sayer et al*. [2016] retrieved above-cloud AOD over the southeast Atlantic. Due to the enhanced aerosol absorption at shorter visible wavelengths, above-cloud aerosols cause a strong reflectance gradient from blue to near-IR spectrum, allowing their detection/retrieval. More direct retrievals of above-cloud aerosols have been made possible from spaceborne lidar data (from CALIPSO) using depolarization and color ratio measurements [*Chand et al*., 2008], aiding in the assessment of above-cloud aerosol radiative impacts. Although various multisensor satellite measurements have provided highly useful information about the distribution of above-cloud absorbing aerosols and their radiative effects, significant uncertainties remain in the retrievals of both overlying aerosols and underlying cloud properties [*Haywood et al*., 2004; *Wilcox et al*., 2009; *Jethva et al*., 2014; *Alfaro-Contreras et al*., 2014; *Kacenelenbogen et al*., 2014; *Meyer et al*., 2013; *Sayer et al*., 2016]. Among the critical parameters affecting above-cloud aerosol radiative impacts are the optical depths of cloud and the overlying aerosol layer, along with aerosol single scattering albedo. For example, large concentrations of smoke with absorbing aerosol (low SSA) located above optically thick clouds have been observed in causing large positive (warming) aerosol radiative forcing above clouds [e.g., *de Graaf et al*., 2012].

The aforementioned studies have addressed above-cloud aerosol characterization using satellite measurements over the southeast Atlantic. Satellite observations certainly provide a unique vantage point to study the extensive and persistent marine stratocumulus cloud decks and the overlying, seasonally persistent absorbing aerosol layer. However, fully considering the radiative interactions between aerosols and clouds would require multiple viewing/azimuthal observations (forward, backward, and side scattering) of the cloud field occurring in the three-dimensional space.

In contrast to the satellite-based studies (focused on above-cloud characterization), here we examine cases where clouds are embedded in smoke primarily using airborne multiangular measurements of radiances. Airborne measurements discussed here were obtained during the Arctic Research of the Composition of the Troposphere from Aircraft and Satellites (ARCTAS) experiment, which took place in Canada in June–July 2008 [*Jacob et al*., 2010; *Cubison et al*., 2011; *Kondo et al*., 2011; *Shinozuka et al*., 2011; *Corr et al*., 2012]. The focus of this work is on measurements from NASA's P-3B aircraft on 30 June 2008 and 2 July 2008, in northern Saskatchewan, Canada, areas that are mostly covered by boreal forest. These flights provided opportunities for detailed in situ observations of flaming fires, plume evolution, and vertical profiles in homogenous fire outflow regions [*Gatebe et al*., 2012]. We use radiance data obtained with a multiwavelength scanning radiometer, Cloud Absorption Radiometer (CAR) [*King et al*., 1986; *Tsay et al*., 1998; *Gatebe et al*., 2012; *Gatebe and King*, 2016], which provides unprecedented detail of the multiangular distribution of radiation scattered from aerosols, clouds, and the surface. Measurements obtained during flights in the "spiraling" mode allowed us to characterize the vertical structure of radiation interactions involving clouds embedded in smoke.

2. Airborne Data Sets

We used measurements acquired from NASA's P-3B aircraft as part of the June–July 2008 ARCTAS experiment. The airborne experiment consisted of a suite of measurements from both remote sensing and in situ instrumentation. Specifically, the P-3B payload included 10 primary instruments [see *Gatebe et al*., 2012] for measuring aerosol optical depth, aerosol extinction and scattering, aerosol size distribution, solar spectral (0.38–2.20 μm) downwelling and upwelling irradiance, broadband downwelling and upwelling solar

(0.20–3.6 μm) and IR (4.5–42 μm) irradiance, angular distribution of scattered radiation in different directions, cloud condensation nuclei, and NO_2 and carbon monoxide concentrations. Here we use calibrated multiangular radiances, broadband irradiances, spectral aerosol optical depths, and aerosol scattering/absorption coefficients, based on coincident measurements from the same flights.

The multiangular radiances are obtained from CAR measurements for nine narrowband wavelengths ranging from UV to shortwave IR (0.34 μm to 2.3 μm), with the radiance absolute accuracy of $<$5% [*Gatebe et al*., 2012]. The CAR mirror scans 360° in a plane perpendicular to the direction of flight, and the data are collected through a 190° field of view (1° instantaneous field of view) [see *Gatebe et al*., 2012]. The 360° azimuthal angles in the processed CAR data are the relative azimuth angles (φ), while the solar zenith angle and the CAR scan/view zenith angle are denoted as θ_o and θ, respectively. The spectral AOD (or τ) data are obtained from NASA Ames 14-Channel Airborne Tracking Sunphotometer (AATS-14) with AOD retrievals at 14 wavelengths from 0.35 μm to 2.1 μm [*Russell et al*., 1999; *Shinozuka et al*., 2011]. In addition, downwelling irradiance measurements were made from solar and IR broadband radiometers (BBRs), which are modified Kipp & Zonen CM-22 pyranometers and CG-4 pyrgeometers, respectively [*Bucholtz et al*., 2010]. The uncertainty in BBR measurements has been reported to be 3–5% (http://airbornescience.nasa.gov/instrument/BBR). Finally, information about aerosol absorption/scattering was obtained from the three-wavelength Radiance Research Particle Soot Absorption Photometers, used to measure light absorption by aerosols at 0.47 μm, 0.53 μm, and 0.66 μm [*Clarke et al*., 2007]. Using the ambient aerosol absorption and scattering coefficients, we calculated the SSA for the midvisible region at 0.53–0.55 μm, used in our 1-D and 3-D radiative transfer calculations.

3. Results

3.1. Analysis of CAR Observations

Figure 1a shows satellite imagery (Aqua/MODIS) of widespread outbreaks of forest fire plumes on 30 June 2008 stretching across hundreds of kilometers over Saskatchewan, with Cold Lake (origin of flight #2016) situated just outside the southwestern edge of the region. Along with the dense smoke in clear-sky (cloud-free regions), scattered clouds are also clearly visible as embedded in thick forest fire smoke (Figures 1b–1d). As seen in photographs taken from the aircraft while circling around a fire outbreak, dense and optically thick plumes of smoke are generated from the boreal forest fires (Figure 1b). A glimpse of clouds mixed with smoke is shown in Figures 1c and 1d. As observed at the TOA in satellite imagery, smoke above clouds appears to induce darkening in cloudy areas (where the smoke-induced enhancement in solar absorption surpasses the enhancement in scattering), in contrast to the cloud-free smoke brightening over vegetation (where the enhancement in scattering dominates). While significant cloud coverage is associated with afternoon convection (Aqua overpass is at ~1:30 P.M. local time); clouds forming near the source of plumes could be attributed to pyroconvective activity resulting in pyrocumulus (pyroCu) clouds. These were the subject of a recent investigation by *Gatebe et al*. [2012], which studied the angular distribution of radiance within the pyroCu and the multiple scattering processes therein.

Two days later on 2 July 2008, measurements from flight #2017 were obtained when the aircraft spiraled down, allowing CAR to take multiangular measurements in 360° azimuthal directions. Details of the flight path and observations' summary are available from http://car.gsfc.nasa.gov/data/index.php?id=113&mis_id=8&n=ARCTAS. The aircraft made three and a half circles at different levels above and within a smoke plume. Figure 2a shows false-color imagery generated from the three CAR channels at 1.04 μm, 0.87 μm, and 0.47 μm. This combination of red, green, and blue colors using different CAR channels helps to visually differentiate clouds from smoke and to see through smoke and identify land surface features such as green vegetation and dark bodies of water [*Gatebe et al*., 2012]. The beginning of the topmost circle is located near the left side of the 2-D imagery, with the solar disk clearly visible in the sky. Here the *x* axis indicates the time traversed during the spiraling descent, and the *y* axis shows the sensor view zenith angles, where 0°–90° show the scattered radiation from sky when the sensor is looking up (0° corresponds to zenith and 90° corresponds to the horizon). From 90° to 180°, the sensor sees reflected radiation from the surface (180° corresponds to nadir). The altitude of the aircraft at the beginning of the topmost circle was 3030 m above mean sea level (msl) (Circle 1 mean altitude is 2700 m above msl), then descended to an altitude of 950 m at the end of the third circle (spiraling farther downward in the partial fourth circle).

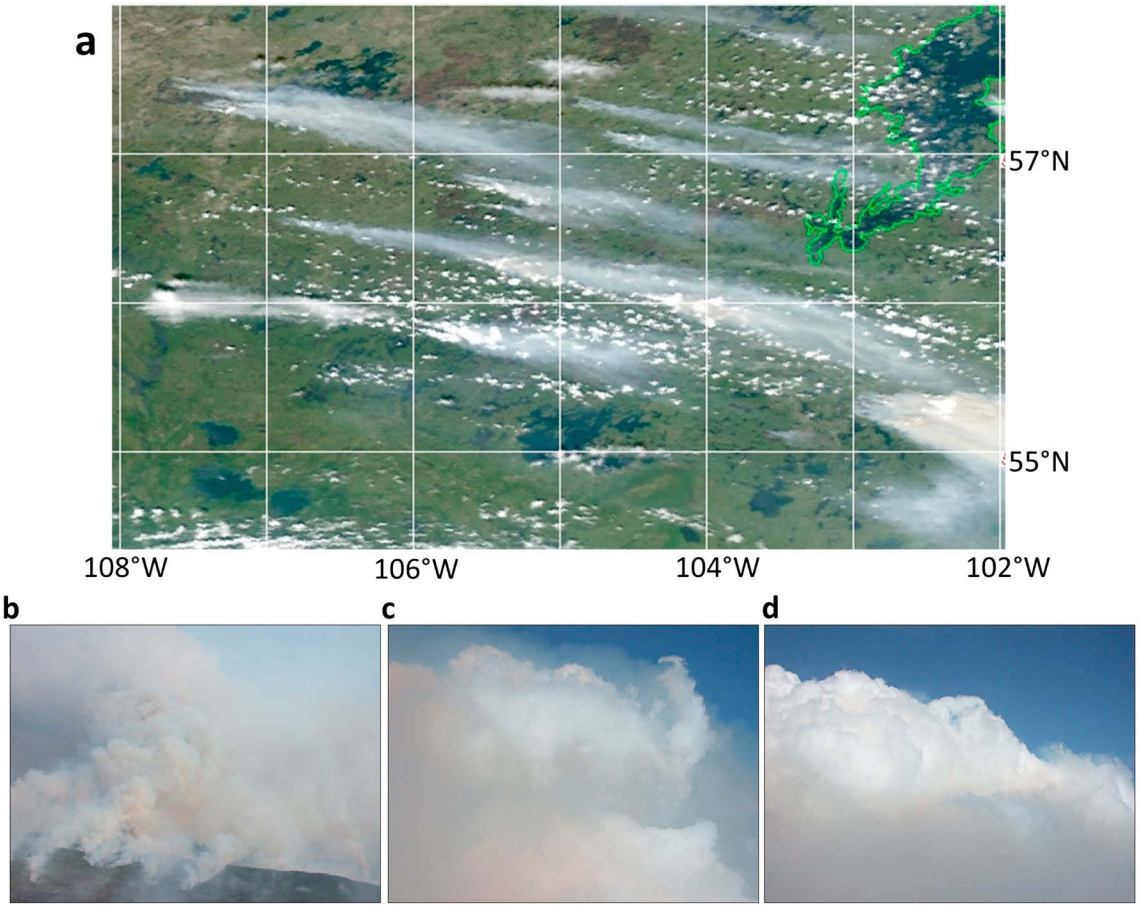

Figure 1. (a) Widespread forest fire smoke plumes on 30 June 2008 (from Aqua/MODIS imagery) stretching across hundreds of kilometers over Saskatchewan, with Cold Lake (origin of flight #2016) situated just outside the southwestern edge of the region. Airborne pictures of (b) forest fire smoke on 30 June 2008 and (c, d) clouds embedded in smoke on 2 July 2008 (flight #2017).

The intensity of scattered radiation significantly strengthened as the aircraft descended to the third and fourth circles, where the smoke plume appears to be optically thick, suggesting that a majority of the dense smoke is located between 1 and 3 km. Additionally, the enhanced forward scattering by smoke particles is evident, especially when viewing the solar disk, at the beginning of the third and fourth circles. Clouds are seen toward the horizon ($60° < \theta < 80°$, $25° < \varphi < 35°$), which appear to be more pronounced during third/fourth circles and may have further evolved during the spiral from Circle 1 to Circle 4, which spans a 10 min period (Figure 2a).

Figure 2b shows the angular distribution of scattered radiation due to smoke as seen by CAR (for sky, $0° < \theta < 90°$) at 0.47 μm. The polar plot shows reflectance ($R_{0.47\mu m}$) derived from Circle 3 for all φ from 0° to 360°, which vary between 0.2 and 0.7. Here the CAR sensor zenith angles (θ) are plotted from the center of the polar plot, increasing toward the periphery of the polar plot, i.e., from 0° to 90°. During the spiral, altitude of the aircraft decreased (nearly monotonically) from the beginning of the Circle 3 at 1582 m ($\varphi = 0°$) to 950 m ($\varphi = 360°$). Both the density and forward scattering nature of the smoke plume is evident in the top right quadrant of the polar plot, with enhanced smoke reflectance values exceeding 0.6, much higher than the relatively smoke-free sky in the backward scattering domain ($R_{0.47\mu m} \sim 0.2$–0.3). To aid the interpretation of $R_{0.47\mu m}$ and its angular distribution shown in the polar plot, we also show the false-color imagery (in polar form) with CAR viewing downward toward surface (from Circle 1), see supporting information Figure S1. As discussed earlier, the majority of the smoke plume is located below the starting altitude of Circle 1. Overall, scattering due to smoke at the shorter wavelengths (e.g., 0.47 μm as observed in Figure 2b) is quite consistent with the pattern of false-color imagery (Figure 2a), resulting in an enhanced blue hue.

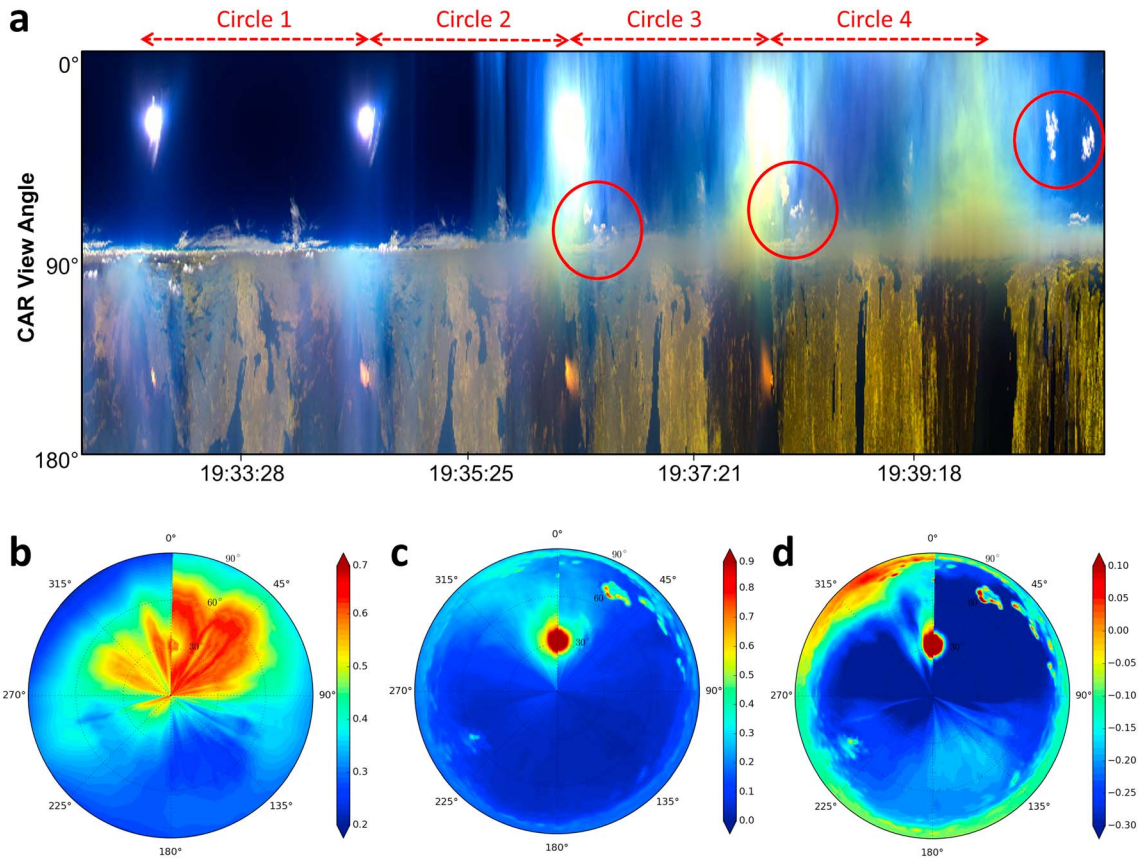

Figure 2. (a) False-color imagery from three CAR channels, with reflectances at 1.04 μm, 0.87 μm, and 0.47 μm displayed with red, green, and blue colors, respectively. Here the *x* axis indicates the time (in UTC) during the circular measurements spiraling down. The *y* axis corresponds to downwelling radiation at the sensor zenith angles from 0° to 90° (0° corresponds to zenith), and upwelling radiation from the surface from 90° to 180°. Angular distribution of scattered radiation in Circle 3 from CAR measurements of sky ($0° < \theta < 90°$) at (b) 0.47 μm, and at (c) 1.66 μm, for all φ from 0° to 360°. (d) Slope of reflectance across six wavelengths from 0.47 μm to 1.66 μm ($dR/d\lambda$) to help differentiate between clouds embedded in smoke (positive slope) and cloud-free smoke (negative slope). In all polar plots, the viewing zenith angle is represented as the radial distance from the center toward the periphery and the azimuth as the arc length on the respective zenith circle. The principal plane is within the 0°–180° azimuthal plane with the Sun located in the 180° azimuthal direction. Using this convention, the upper half of the polar plots represents forward scattering and the lower half backscattering.

The presence of clouds appears to be masked by the strong scattering of smoke particles at 0.47 μm, which prompted us to analyze the reflectance at longer wavelengths. For instance at 1.66 μm, the smoke plume is nearly transparent, whereas the presence of clouds is evident as enhanced scattering is seen around the periphery, with $R_{1.66\mu m} > 0.7$ ($60° < \theta < 80°$, $25° < \varphi < 35°$) (Figure 2c). The fact that clouds are not visible at the shorter wavelengths also suggests darkening, especially around blue wavelengths, as these clouds are embedded in thick smoke. To further highlight the impact of clouds embedded in smoke, we calculated the slope of reflectance across six wavelengths from 0.47 μm to 1.66 μm ($dR/d\lambda$), to readily differentiate between clouds and cloud-free smoke. For instance, the dark blue region in the first quadrant of Figure 2d represents smoke associated with a strong negative slope value of 0.3, in contrast to the positive slope (exceeding 0.1) for clouds embedded in smoke. In other words, the spectral reflectance of smoke is observed to strongly decrease with increasing wavelength, whereas clouds embedded in smoke are characterized by an increasing gradient. These observations of the spectral reflectance gradient, mapped onto the polar plot, not only help to provide semiquantitative information of smoke loading but also help us to detect clouds in the presence of smoke.

Spectral observations for smoke-only conditions are also studied, when viewing the sky (Figure 3a) and vegetated surface (Figure 3b). As a case study from flight #2017/Circle 3, Figure 3a show the spectral reflectance at eight channels from 0.34 μm to 1.27 μm, for varying azimuthal angles ($45° < \varphi < 270°$) at a fixed viewing zenith angle ($\theta = 60°$). The smoke reflectance is observed to be systematically decreasing from shorter visible

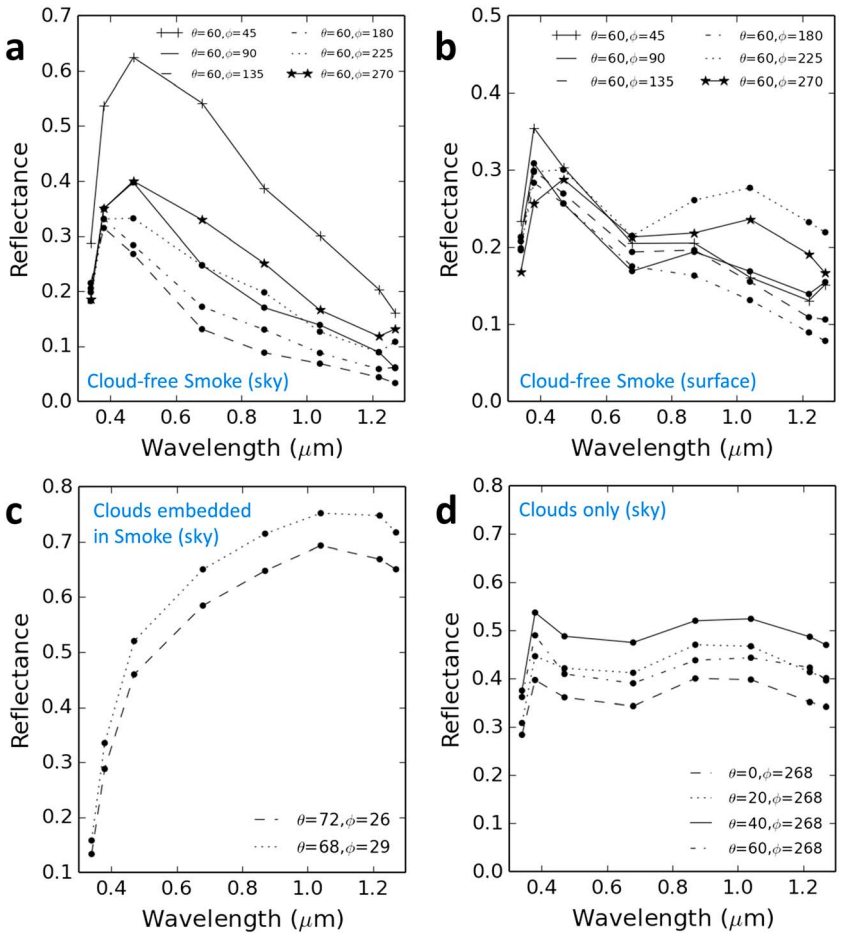

Figure 3. CAR spectral observations for smoke-only conditions in the (a) sky and over (b) vegetated surface, from flight #2017/Circle 3, for varying azimuthal angles ($45° < \varphi < 270°$) at a fixed viewing zenith angle ($\theta = 60°$). Spectral reflectance from sky measurements of (c) clouds embedded in smoke from flight #2017/Circle 3, indicating the characteristic VIS-NIR gradient, and (d) clouds outside of the smoke plume region with a flat spectral signature.

wavelengths (0.47 μm) toward longer wavelengths (this decrease is typically associated with presence of fine particles), which is consistent with the strong negative gradients indicated by Figure 2d. The strong forward scattering of aerosols and the resulting enhanced reflectance is evident in the spectral reflectance curves (Figure 3a) being highest at smallest azimuth angle ($\varphi = 45°$), whereas lower reflectances are observed in the backward scattering domain (e.g., $\varphi = 180°$).

Similarly, a negative slope is also found for CAR spectral reflectance measurements over the surface (Figure 3b), which is mostly dominated by vegetation/forest cover (with some water bodies also present in the mixed scene). In general, a decreasing tendency is systematically observed from blue to red channels, while there is an increase in reflectance at NIR wavelengths suggesting the apparent presence of vegetation. These measurements are obtained from the topmost Circle 1 overlooking the surface (with smoke between the aircraft level and surface). The altitude of the aircraft varied from 3030 m to 2310 m during the Circle 1 spiral. Considering the vegetated surface below, one would expect lower reflectance values at shorter wavelengths (e.g., blue bands) in comparison to much higher reflectances at longer wavelengths (e.g., NIR bands). However, the observations depicted in Figure 3b are during the presence of heavy smoke aerosols over a vegetated surface. Since vegetated surface is relatively dark at shorter wavelengths, the enhanced reflectance observed by the sensor is associated with smoke aerosol scattering. Therefore, due to the aerosol-induced enhancement at shorter wavelengths, comparable or even higher values of reflectance are observed at the blue channel (0.47 μm) relative to NIR channels (0.87 μm and 1.04 μm).

It is interesting to note here (Figures 3a and 3b) the increase in reflectance across the UV channels (in some cases from UV to blue, i.e., from 0.34 μm to 0.47 μm), suggesting enhanced absorption toward the UV wavelengths. This spectral absorption occurring in the UV could be due to the significant presence of organic aerosols found in biomass burning smoke plumes as reported by several in situ studies from ARCTAS/Canada measurements [*Kondo et al*., 2011; *Cubison et al*., 2011; *Corr et al*., 2012]. In fact, in their ARCTAS study, *Kondo et al*. [2011] concluded that organic aerosols constituted the majority of aerosol mass (in the submicron range) in biomass burning wildfire smoke plumes. In addition, *Corr et al*. [2012] reported strong spectral absorption associated with biomass burning aerosols with 2–3 times larger absorption in the UV wavelengths than in blue, primarily due to organics in the ARCTAS/Canada and California plumes. In an earlier study, widespread organic aerosol concentrations have also been reported over marine stratocumulus cloud decks off the coast of California [*Sorooshian et al*., 2007]. Organic aerosols found in biomass burning smoke are widely recognized to exhibit strong wavelength dependence, approximately λ^{-2}, with enhanced light absorption in the UV [*Kirchstetter et al*., 2004]. Overall, these studies point to the strong possibility of organics causing our observations of reduced UV reflectances for smoke.

In contrast to the negative slope across blue to NIR spectrum for (cloud-free) smoke aerosols, clouds embedded in smoke show a characteristic positive gradient, with reduced reflectances in the shorter wavelengths (Figure 3c). Especially low values were observed for UV and blue reflectance ($R_{0.34\mu m} < 0.2$ and $R_{0.47\mu m}$ ~0.5), as opposed to higher reflectances ~0.7 in the NIR channels (e.g., 1.03 μm). Due to the enhanced absorption at shorter (UV and blue) wavelengths, clouds embedded in smoke appear darker, resulting in a strong reflectance gradient across UV-VIS-NIR. These observations are for the broken cloud cover found in the periphery of the polar plot and previously seen in the false-color imagery (Figure 2). We also studied the spectral reflectance of clouds not impacted by the influence of smoke (i.e., outside of the pyroconvective region), during the flight #2016 track, which shows a relatively flat reflectance spectrum across VIS-NIR (Figure 3d). These observations from a "clean" cloud are expected when viewed in the absence of smoke, as clouds are typically spectrally invariant up to NIR.

In addition to darkening of clouds observed during the spirals, similar cases were found elsewhere from the same flight during a linear transect (when there was little variation in the altitude of the aircraft). Figure 4 shows optically thick continuous cloud cover embedded in smoke, seen as yellowing hue in the false-color imagery, from flight #2016. Thick smoke is prevalent near the underlying surface and extends to elevated altitudes above aircraft level (the aircraft altitude is around 810 m). To derive more quantitative insight, we extracted spectral reflectances over two transects in the cloud-free smoke (transect 1) and cloud mixed with smoke (transect 2) in the sky. Unlike the clouds (mixed with smoke) viewed at oblique angles (found in the periphery of the polar plot, Figure 2d), the Sun-sensor geometry in the case of two transects is fixed at $\theta = 31°$, $\varphi = 52°$, and $\theta_o = 34°$ (Figure 4, inset). Spectral reflectances for clouds embedded in smoke show the characteristic positive slope across UV-VIS-NIR (transect 2), whereas a general decreasing pattern occurs in the case of smoke (transect 1). The shaded areas in Figure 4 (inset) represent the ±1 standard deviation of spectral reflectances from 0.34 μm to 1.27 μm.

3.2. The 1-D and 3-D Radiative Transfer Simulations

We also used a 1-D radiative transfer (RT) model to simulate the observed darkening of clouds embedded in smoke at shorter wavelengths. Here the Discrete Ordinates Radiative Transfer (DISORT) model [*Stamnes et al*., 1988] was used to calculate reflectances at eight wavelengths from 0.34 μm to 1.27 μm for "smoke mixed with cloud" and "clean cloud" scenarios (Figure 5). In our RT calculations, we set $\theta = 110°$ as the downwelling radiation is propagating in the lower hemisphere toward the sensor ($\theta = 110°$ in DISORT is equivalent to the CAR scan angle of $\theta = 70°$), with $\theta_o = 33°$ and $\varphi = 26°$, similar to CAR measurements from flight #2017/Circle 3 on 2 July 2008 (Figure 3c). The top layer in the RT calculations corresponds to a cloud layer, while the aerosol layer is placed between the cloud and sensor. Given this configuration, the performed calculations essentially are transmittance calculations as the sensor is measuring the radiance below the cloud and aerosol layers. However, to be consistent throughout the paper, we refer to the transmittance as reflectance even when the sensor measures downwelling radiance viewing the cloud-free/cloudy sky. The Legendre coefficients input to the RT model were calculated from *Wiscombe's* [1980] Mie code for spherical cloud droplets with a modified gamma size distribution and for aerosols with a lognormal size distribution. The Mie phase function calculations were performed for varying cloud effective radius (CER) from 8 μm to 12 μm.

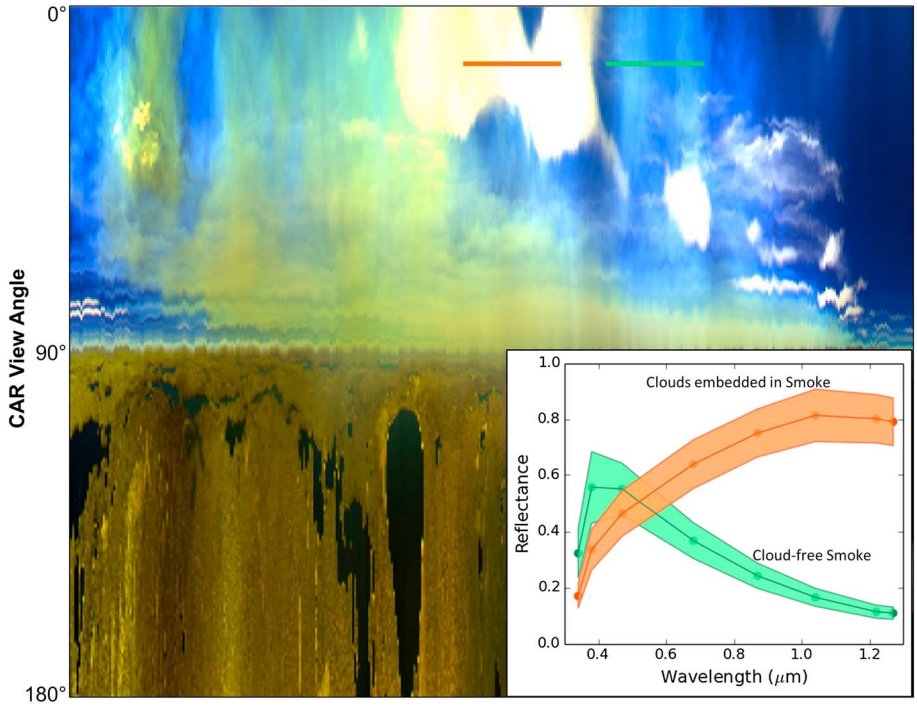

Figure 4. CAR observations of optically thick clouds embedded in smoke revealed by a yellowing hue in the false-color imagery, from flight #2016 on 30 June 2008. (inset) Spectral reflectances over two transects in the cloud-free smoke (green) and cloud mixed with smoke (brown) regions in the sky. Sun-sensor geometry for the two transects is given by $\theta = 31°$, $\varphi = 52°$, and $\theta_o = 34°$. Shaded area represents the ±1 standard deviation of spectral reflectances from 0.34 μm to 1.27 μm.

A reference vegetation surface reflectance spectra was used in the RT calculations, assuming a Lambertian reflector, as we are only simulating the sky reflectance.

In order to focus on aerosol radiative effects, no water vapor absorption and Rayleigh scattering inputs were provided to DISORT. The aerosol single scattering albedo at 0.55 μm was set to 0.88, based on the mean single scattering albedo obtained from the coincident measurements of scattering and absorption coefficients from in situ measurements (from Circle 1 to Circle 3), on board the P-3 aircraft, alongside CAR measurements. In Figure 5a, RT-calculated reflectances are shown for a cloud optical depth of 5 and CER of 8 μm, with the optical depth of the aerosol layer varying from 0 to 1.5. In contrast to the relatively insensitive NIR

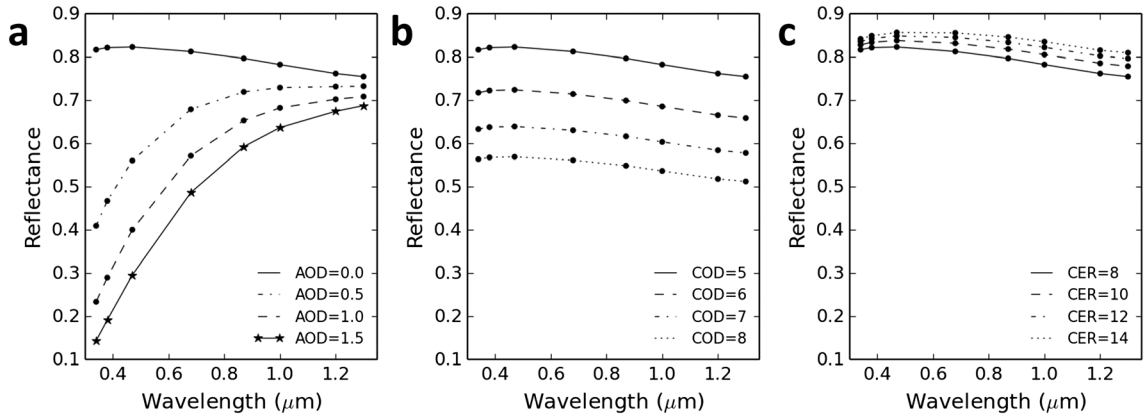

Figure 5. The 1-D RT sensitivity calculations of spectral reflectance for (a) smoke mixed with cloud and (b, c) clean cloud scenarios (no aerosol input), with Sun-sensor geometry similar to CAR measurements from flight #2017 on 2 July 2008 ($\theta_o = 33°$, $\theta = 70°$, and $\varphi = 26°$). In the 1-D calculations, θ is set to 110° as the radiation is propagating in the lower hemisphere toward the sensor (equivalent to the CAR scan angle, $\theta = 70°$). Radiance calculations were performed by varying (Figure 5a) AOD from 0 to 1.5 at 0.5 μm with fixed COD = 5 and CER = 8 μm, (Figure 5b) COD from 5 to 8 (no aerosol and CER = 8 μm), and (Figure 5c) CER from 8 to 14 μm (no aerosol and COD = 5).

wavelengths (>1 μm), reflectance at the UV-VIS bands are associated with enhanced absorption, resulting in a significant positive gradient (Figure 5a), as also observed from CAR measurements. Essentially, the area between the two curves for AOD = 0 and AOD = 1.5 denotes the energy absorbed by the smoke layer between the sensor and cloud. The characteristic UV-VIS-NIR gradient is similar to that for aerosols above marine stratocumulus decks over the southeast Atlantic, apparent in spaceborne measurements from the hyperspectral SCIAMACHY and multispectral MODIS instruments [*de Graaf et al*., 2012; *Jethva et al*., 2013]. Note that in supporting information Figure S2, we also show the impact of aerosol absorption on cloud darkening, with the sensor viewing the cloud from top and smoke present above the cloud layer, similar to a satellite TOA perspective. The darkening induced by aerosol absorption is amplified with increasing cloud layer thickness due to enhanced interactions between a bright surface (clouds) and an overlaying absorbing medium (smoke).

Also shown in Figure 5 are scenarios when the aerosol layer is absent with only clouds viewed from the sensor, for varying cloud optical depth (COD) from 5 to 8 (Figure 5b) and CER from 8 μm to 14 μm (Figure 5c). Without the presence of aerosols, as expected, reflectances at the longer (NIR) wavelengths are most sensitive to variations in cloud droplet size (COD fixed at 8 in Figure 5c), whereas the sensitivity to varying optical depths (COD from 5 to 8) results in significant perturbations in the entire UV-NIR range in Figure 5b. However, the shape of spectral reflectance remains flat, suggesting a uniform change in the brightness of cloud in response to its varying thickness.

Furthermore, we performed 3-D RT model calculations toward a more realistic characterization of CAR-observed reflectances, as the clouds visible in Figures 2 and 3 are clearly not occurring in homogeneous layers. We employ 3-D RT simulations using the Monte Carlo technique [e.g., *Marchuk et al*., 1980]. The Monte Carlo model is a modified version of the code used in several earlier studies, including *Várnai and Marshak* [2002], and has also been tested in the Intercomparison of 3-D Radiation Codes project [*Cahalan et al*., 2005]. The actual code used in this study was also tested for 1-D calculations through comparisons with the DISORT model. In order to restrict simulation uncertainties under 0.5%, each result is based on 4 million photon trajectories in backward Monte Carlo simulations.

The Monte Carlo setup includes the altitude difference between the aircraft at 1 km and cloud base at 2 km. The viewing zenith angle of 70° (20° above the horizon) is similar to the CAR measurements and the 1-D calculations and implies a horizontal distance between the sensor and the cloud of about 2.7 km. The cloud size was assumed to be of 3 km × 3 km × 1 km, whereas the instrument position (km) was fixed at $x = 0$, $y = 1$, and $z = 1$ in the 3-D space. We placed the cloud extent (km) within $x = 4$–7, $y = 1$–4, and $z = 2$–3, and given the observational Sun-sensor geometry, the sensor essentially is viewing the side of the cloud at an oblique angle (with the sensor positioned below the cloud layer). For simplicity, results shown here correspond to cloud absorption kept at 0 and COD fixed at 8 (we performed calculations for varying COD from 5 to 8 without any significant changes to the spectral reflectance shape for different CODs). All simulations used CER of 8 μm. Additionally, the cloud scattering phase function was allowed to vary slightly with wavelength according to Mie theory. The aerosol layer was placed between the sensor and the cloud field, and calculations were performed for spectral AOD shown in Figure 7b, with AOD at ~0.5 μm of 1.5, obtained from spectral AOD measurements coincident with CAR (Figure b). Based on data from Circle 3, spectral AOD at 0.35 μm and 1.6 μm ranged from 2.85 ± 1.35 to 0.18 ± 0.11.

The results of Monte Carlo simulations are shown in Figure 6, where a strong positive gradient is associated with the absorbing aerosol layer present between the sensor and cloud field (red). The simulated spectral reflectance mimics the CAR observations previously seen in Figure 3c. The large aerosol absorption impact in the UV-blue spectrum is seen in the simulated low reflectance values of 0.23 and 0.55 at 0.34 μm and 0.47 μm, respectively. This is in sharp contrast to a clean cloud scenario where the 3-D simulations also point to a flat spectral shape (blue). As expected, the radiative effect of aerosols significantly reduces at NIR wavelengths, where the two curves start to converge around 1.2 μm. In these simulations the aerosol SSA was 0.81 at 0.34 μm, 0.84 at 0.38 μm, and 0.88 at 0.47 μm (based on ABS measurements); a linear interpolation was used to reach SSA = 1.0 at 1.6 μm. The asymmetry parameter was considered to be wavelength dependent, varying from 0.7 at 0.34 μm, 0.6 at 0.5 μm, and ~0.3 at 1.6 μm. These calculations did not consider any Rayleigh scattering inputs. Inclusion of Rayleigh scattering resulted in a small decrease in reflectances at the shorter wavelengths, e.g., further reducing the value at 0.34 μm from 0.23 to 0.15 (not shown). Overall,

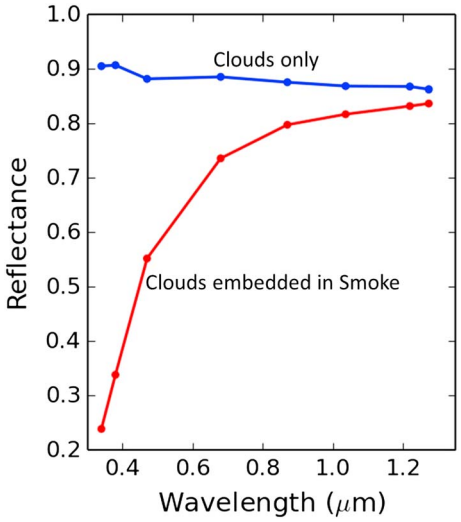

Figure 6. Monte Carlo 3-D radiative transfer calculations for cloud only (blue) and smoke mixed with cloud (red), indicating flat spectrum for clouds and a strong spectral gradient associated with cloud darkening, respectively. Reflectance calculations were performed for AOD of 1.5 at ~0.5 μm, obtained from spectral AOD measurements from AATS, coincident with CAR.

based on the Monte Carlo results in this study, the 3-D effects did not change the qualitative behavior of cloud-aerosol radiative interactions. While the basic behavior remained the same (in comparison to 1-D calculations), as noted above there were some quantitative changes due to the 3-D setup that affected the specific reflectance values.

4. Discussion and Summary

Overall, the moderately absorbing smoke (with mean SSA of 0.88 ± 0.19 at 0.53 μm) coupled with high AOD (1.5 ± 0.7 at ~0.5 μm) leads to significant solar absorption, suggesting a large direct aerosol radiative effect in the presence of clouds. We also retrieved AOD and SSA using a bidirectional reflectance model [*Ahmad and Deering*, 1992] that took all the available angular reflectance measurements from CAR as input (see supporting information). This model provides an approximate solution based on analytical functions and is capable of detecting hot spot and specular reflectance of the underlying vegetated surface. The AOD retrieved here corresponds to the entire column from the aircraft down to the surface level. The approximation yielded a close agreement with the observed data (SSA retrieved within 0.86–0.89, and AOD within 1.21–1.81 at 0.47 μm), as discussed in the supporting information.

In addition to simultaneous measurements from CAR and AATS (and aerosol absorption), coincident downwelling solar irradiance measurements from a broadband radiometer at the aircraft level also provided an independent estimate of the direct aerosol radiative effect. Figure 7a shows downwelling irradiance ($W\,m^{-2}$) as a function of AOD at 0.52 μm from the AATS, both obtained during nearly coincident measurements from Circle 3. A total of 26 direct Sun measurements yielded in corresponding AOD ranging from 0.6 to 3.2, available from Circle 3 (Figure 7b). The instantaneous aerosol radiative forcing efficiency, from

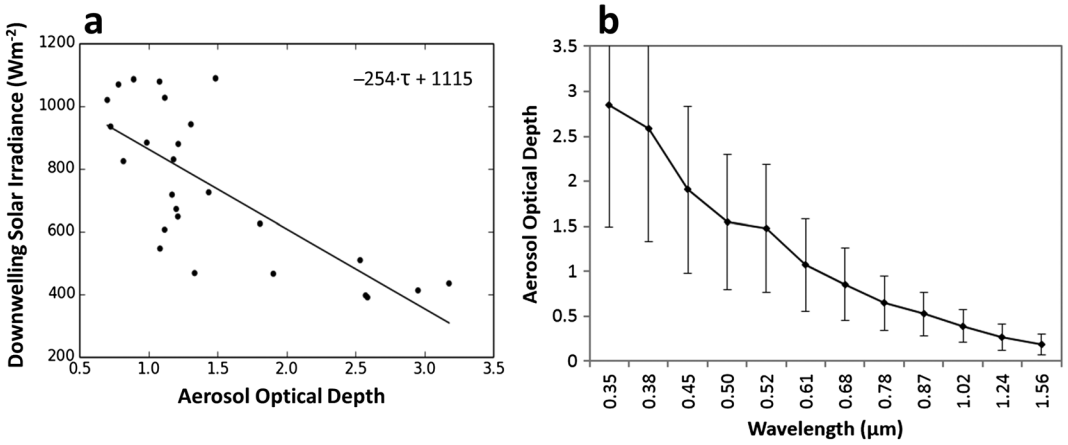

Figure 7. (a) Instantaneous aerosol radiative forcing efficiency of 254 ± 47 $W\,m^{-2}\,\tau^{-1}$ (flux per unit aerosol optical depth) derived from coincident measurements from AATS and BBR at the aircraft level/Circle 3, with AOD at ~0.5 μm. (b) Spectral AOD measurements from the AATS instrument, coincident with CAR data. The average AOD for the entire Circle 3 is 1.5 ± 0.7 at ~0.5 μm, while the spectral AOD from 0.35 μm to 1.6 μm ranged from 2.85 ± 1.35 to 0.18 ± 0.11. The error bars represent the standard deviation of AOD values.

colocated AOD and flux measurements, can be approximated as $254 \pm 47\,\mathrm{W\,m^{-2}}\,\tau^{-1}$, indicated by the slope of the linear regression between AOD and downwelling irradiance. The flux data were normalized by the cosine of the solar zenith angle, though there was little variation in θ_o of around 33°, as the Circle 3 measurements spanned a short time period of ~2 min. In response to the variations in AOD from 0.6 to 3.2, there is a large reduction of downwelling irradiance from ~1100 $\mathrm{W\,m^{-2}}$ to ~400 $\mathrm{W\,m^{-2}}$. Although the radiative forcing efficiency estimate is based on a linear fit, we use caution here with our reported efficiency value as the flux measurements were obtained during the spiral descent. The flux data have not been corrected for the attitude of the aircraft as these corrections are particularly difficult to make during a spiral (A. Bucholtz, Naval Research Laboratory, personal communication, 2016).

One of the widely recognized pathways of cloud and aerosol radiative interactions is through the semidirect effect, where the radiative heating due to absorbing aerosols (e.g., soot) may lead to changes in cloud cover [e.g., *Ackerman et al*., 2000]. For example, the Indian Ocean Experiment study by *Ackerman et al*. [2000] showed reduction in cloudiness due to atmospheric warming induced by black carbon aerosols, leading to cloud burnoff. The semidirect effect of absorbing aerosols may also depend on the vertical distribution/location of aerosols in the presence of clouds. Absorbing aerosols found above stratocumulus cloud decks darken the scene at TOA, but the aerosol-induced warming above clouds acts to lower cloud top entrainment rate thereby enhancing cloud cover [*Johnson et al*., 2004; *Wilcox*, 2010], in contrast to the cloud burnoff response. Based on the cases studied in this ARCTAS analysis, "clouds embedded in absorbing aerosols" are likely to have relevance to the cloud burnoff semidirect effect. We have also carried out preliminary analysis of smoke aerosols above marine stratocumulus clouds using CAR multiangular measurements from the Southern African Regional Science Initiative-2000 (SAFARI) campaign. Based on the limited available cases studied from the ARCTAS and SAFARI data, the radiative signature of clouds embedded in absorbing aerosols and above-cloud aerosols appears to be similar, suggesting aerosol-induced warming both above and within the cloud layer. However, the varying magnitudes of absorbing aerosol-induced warming within or above clouds may be important in determining the relative impacts of semidirect effects on the net changes in cloud cover and properties.

To summarize, here we used multiangular airborne measurements (in spiraling mode), to demonstrate the complexity of the strongly coupled aerosol-cloud system, from a three-dimensional radiation perspective. In particular, CAR observations allowed us to characterize the angular distribution of optically thick smoke, where clouds embedded in wildfire smoke were found to be associated with a strong UV-VIS-NIR spectral gradient. The largest darkening by smoke was found in the UV/VIS, with reflectance at 0.34 μm reducing to 0.2 (or 20%), in contrast to 0.8 at NIR wavelengths (e.g., 1.27 μm). Results presented in this study also include observations in the side-scattering domain, with potential implications to aerosol-induced semidirect effects as well as to retrievals of cloud droplet size from side-scanning remote sensing [*Martins et al*., 2011]. Our observations of smoke-cloud radiative interactions were found to be physically consistent with theoretical 1-D and 3-D radiative transfer calculations, capturing the observed spectral gradients. This work also suggests the importance of multiangular radiation measurements toward a future potential closure investigation to fully study the aerosol-cloud-radiation interactions, in combination with in situ observations of aerosol/cloud microphysics.

Acknowledgments
This research is supported by NASA Radiation Sciences program, managed by Hal Maring. We are grateful to several instrument Principal Investigators for the provision of airborne data used in this study: Jens Redemann/NASA ARC (spectral AOD data from AATS measurements), Anthony Bucholtz/NRL, Monterey (solar radiation flux data from BBR measurements), and Antony Clarke/University of Hawaii (in situ aerosol optical properties). Data sets used in this paper are available from the ARCTAS data archive at http://www-air.larc.nasa.gov/missions/arctas/arctas.html and CAR data archive at http://car.gsfc.nasa.gov/. We thank three anonymous reviewers for their comments and suggestions which helped improve an earlier version of the manuscript.

References

Ackerman, A. S., O. B. Toon, D. E. Stevens, A. J. Heymsfield, V. Ramanathan, and E. J. Welton (2000), Reduction of tropical cloudiness by soot, *Science*, *288*, 1042–1047.

Adebiyi, A. A., P. Zuidema, and S. J. Abel (2015), The convolution of dynamics and moisture with the presence of shortwave absorbing aerosols over the southeast Atlantic, *J. Clim.*, *28*(5), 1997–2024, doi:10.1175/JCLI-D-14-00352.1.

Ahmad, S. P., and D. W. Deering (1992), A simple analytical function for bidirectional reflectance, *J. Geophys. Res.*, *97*, 18,867–18,886, doi:10.1029/92JD01624.

Alfaro-Contreras, R., J. Zhang, J. R. Campbell, R. E. Holz, and J. S. Reid (2014), Evaluating the impact of aerosol particles above cloud on cloud optical depth retrievals from MODIS, *J. Geophys. Res. Atmos.*, *119*, 5410–5423, doi:10.1002/2013JD021270.

Bucholtz, A., D. L. Hlavka, M. J. McGill, K. S. Schmidt, P. Pilewskie, S. M. Davis, E. A. Reid, and A. L. Walker (2010), Directly measured heating rates of a tropical subvisible cirrus cloud, *J. Geophys. Res.*, *115*, D00J09, doi:10.1029/2009JD013128.

Cahalan, R. F., et al. (2005), The I3RC—Bringing together the most advanced radiative transfer tools for cloudy atmospheres, *Bull. Am. Meteorol. Soc.*, *86*, 1275–1293.

Chand, D., T. L. Anderson, R. Wood, R. J. Charlson, Y. Hu, Z. Liu, and M. Vaughan (2008), Quantifying above-cloud aerosol using spaceborne lidar for improved understanding of cloudy sky direct climate forcing, *J. Geophys. Res.*, *113*, D13206, doi:10.1029/2007JD009433.

Chand, D., R. Wood, T. L. Anderson, S. K. Satheesh, and R. J. Charlson (2009), Satellite-derived direct radiative effect of aerosols dependent on cloud cover, *Nat. Geosci.*, *2*(3), 181–184, doi:10.1038/ngeo437.

Clarke, A., et al. (2007), Biomass burning and pollution aerosol over North America: Organic components and their influence on spectral optical properties and humidification response, *J. Geophys. Res.*, *112*, D12S18, doi:10.1029/2006JD007777.

Corr, C. A., S. R. Hall, K. Ullmann, B. E. Anderson, A. J. Beyersdorf, K. L. Thornhill, M. J. Cubison, J. L. Jimenez, A. Wisthaler, and J. E. Dibb (2012), Spectral absorption of biomass burning aerosol determined from retrieved single scattering albedo during ARCTAS, *Atmos. Chem. Phys.*, *12*(21), 10,505–10,518, doi:10.5194/acp-12-10505-2012.

Cubison, M. J., et al. (2011), Effects of aging on organic aerosol from open biomass burning smoke in aircraft and laboratory studies, *Atmos. Chem. Phys.*, *11*(23), 12,049–12,064, doi:10.5194/acp-11-12049-2011.

de Graaf, M., L. G. Tilstra, P. Wang, and P. Stammes (2012), Retrieval of the aerosol direct radiative effect over clouds from spaceborne spectrometry, *J. Geophys. Res.*, *117*, D07207, doi:10.1029/2011JD017160.

Feng, N., and S. A. Christopher (2015), Measurement-based estimates of direct radiative effects of absorbing aerosols above clouds, *J. Geophys. Res. Atmos.*, *120*, 6908–6921, doi:10.1002/2015JD023252.

Gatebe, C., T. Varnai, R. Poudyal, C. Ichoku, and M. King (2012), Taking the pulse of pyrocumulus clouds, *Atmos. Environ.*, *52*, 121–130.

Gatebe, C. K., and M. D. King (2016), Airborne spectral BRDF of various surface types (ocean, vegetation, snow, desert, wetlands, cloud decks, smoke layers) for remote sensing applications, *Remote Sens. Environ.*, *179*, 131–148, doi:10.1016/j.rse.2016.03.029.

Haywood, J. M., S. R. Osborne, and S. J. Abel (2004), The effect of overlying absorbing aerosol layers on remote sensing retrievals of cloud effective radius and cloud optical depth, *Q. J. R. Meteorol. Soc.*, *130*(598), 779–800, doi:10.1256/qj.03.100.

Hsu, N. C., J. R. Herman, and S.-C. Tsay (2003), Radiative impacts from biomass burning in the presence of clouds during boreal spring in southeast Asia, *Geophys. Res. Lett.*, *30*(5), 1224, doi:10.1029/2002GL016485.

Jacob, D. J., et al. (2010), The Arctic Research of the Composition of the Troposphere from Aircraft and Satellites (ARCTAS) mission: Design, execution, and first results, *Atmos. Chem. Phys.*, *10*(11), 5191–5212, doi:10.5194/acp-10-5191-2010.

Jethva, H., O. Torres, L. A. Remer, and P. K. Bhartia (2013), A color ratio method for simultaneous retrieval of aerosol and cloud optical thickness of above-cloud absorbing aerosols from passive sensors: Application to MODIS measurements, *IEEE Trans. Geosci. Remote Sens.*, *51*(7), 3862–3870, doi:10.1109/TGRS.2012.2230008.

Jethva, H., O. Torres, F. Waquet, D. Chand, and Y. Hu (2014), How do A-train sensors intercompare in the retrieval of above-cloud aerosol optical depth? A case study-based assessment, *Geophys. Res. Lett.*, *41*, 186–192, doi:10.1002/2013GL058405.

Johnson, B. T., K. P. Shine, and P. M. Forster (2004), The semi-direct aerosol effect: Impact of absorbing aerosols on marine stratocumulus, *Q. J. R. Meteorol. Soc.*, *30*, 1407–1422.

Kacenelenbogen, M., J. Redemann, M. A. Vaughan, A. H. Omar, P. B. Russell, S. Burton, R. R. Rogers, R. A. Ferrare, and C. A. Hostetler (2014), An evaluation of CALIOP/CALIPSO's aerosol-above-cloud detection and retrieval capability over North America, *J. Geophys. Res. Atmos.*, *119*, 230–244, doi:10.1002/2013JD020178.

King, M. D., M. G. Strange, P. Leone, and L. R. Blaine (1986), Multiwavelength scanning radiometer for airborne measurements of scattered radiation within clouds, *J. Atmos. Oceanic Tech.*, *3*, 513–522, doi:10.1175/15200426(1986)003<0513:MSRFAM>2.0.CO;2.

Kirchstetter, T. W., T. Novakov, and P. V. Hobbs (2004), Evidence that the spectral dependence of light absorption by aerosols is affected by organic carbon, *J. Geophys. Res.*, *109*, D21208, doi:10.1029/2004JD004999.

Kondo, Y., et al. (2011), Emissions of black carbon, organic, and inorganic aerosols from biomass burning in North America and Asia in 2008, *J. Geophys. Res.*, *116*, D08204, doi:10.1029/2010JD015152.

Marchuk, G., G. Mikhailov, M. Nazarahev, R. Darbinjan, B. Kargin, and B. Elepov (1980), *The Monte Carlo Methods in Atmospheric Optics*, Springer, New York.

Martins, J. V., A. Marshak, L. A. Remer, D. Rosenfeld, Y. J. Kaufman, R. Fernandez-Borda, I. Koren, A. L. Correia, V. Zubko, and P. Artaxo (2011), Remote sensing the vertical profile of cloud droplet effective radius, thermodynamic phase, and temperature, *Atmos. Chem. Phys.*, *11*, 9485–9501, doi:10.5194/acp-11-9485-2011.

Meyer, K., S. Platnick, L. Oreopoulos, and D. Lee (2013), Estimating the direct radiative effect of absorbing aerosols overlying marine boundary layer clouds in the southeast Atlantic using MODIS and CALIOP, *J. Geophys. Res. Atmos.*, *118*, 4801–4815, doi:10.1002/jgrd.50449.

Meyer, K., S. Platnick, and Z. Zhang (2015), Simultaneously inferring above-cloud absorbing aerosol optical thickness and underlying liquid phase cloud optical and microphysical properties using MODIS, *J. Geophys. Res. Atmos.*, *120*, 5524–5547, doi:10.1002/2015JD023128.

Peers, F., F. Waquet, C. Cornet, P. Dubuisson, F. Ducos, P. Goloub, F. Szczap, D. Tanr'e, and F. Thieuleux (2015), Absorption of aerosols above clouds from POLDER/PARASOL measurements and estimation of their direct radiative effect, *Atmos. Chem. Phys.*, *15*(8), 4179–4196, doi:10.5194/acp-15-4179-2015.

Russell, P. B., J. M. Livingston, P. Hignett, S. Kinne, J. Wong, A. Chien, R. Bergstrom, P. Durkee, and P. V. Hobbs (1999), Aerosol-induced radiative flux changes off the United States mid-Atlantic coast: Comparison of values calculated from Sunphotometer and in situ data with those measured by airborne pyranometer, *J. Geophys. Res.*, *104*(D2), 2289–2307, doi:10.1029/1998JD200025.

Sayer, A. M., N. C. Hsu, C. Bettenhausen, J. Lee, J. Redemann, B. Schmid, and Y. Shinozuka (2016), Extending "Deep Blue" aerosol retrieval coverage to cases of absorbing aerosols above clouds: Sensitivity analysis and first case studies, *J. Geophys. Res. Atmos.*, *121*, 4830–4854, doi:10.1002/2015JD024729.

Shinozuka, Y., et al. (2011), Airborne observation of aerosol optical depth during ARCTAS: Vertical profiles, inter-comparison and fine-mode fraction, *Atmos. Chem. Phys.*, *11*(8), 3673–3688, doi:10.5194/acp-11-3673-2011.

Sorooshian, A., M. L. Lu, F. J. Brechtel, H. Jonsson, G. Feingold, R. C. Flagan, and J. H. Seinfeld (2007), On the source of organic acid aerosol layers above clouds, *Environ. Sci. Technol.*, *41*(13), 4647–4654, doi:10.1021/es0630442, pMID: 17695910.

Stamnes, K., S. C. Tsay, W. Wiscombe, and K. Jayaweera (1988), Numerically stable algorithm for discrete ordinate-method radiative transfer in multiple scattering and emitting layered media, *Appl. Opt.*, *27*, 2502–2509.

Torres, O., H. Jethva, and P. K. Bhartia (2012), Retrieval of aerosol optical depth above clouds from OMI observations: Sensitivity analysis and case studies, *J. Atmos. Sci.*, *69*(3), 1037–1053, doi:10.1175/JAS-D-11-0130.1.

Tsay, S.-C., M. D. King, G. T. Arnold, and J. Y. Li (1998), Airborne spectral measurements of surface anisotropy during SCAR-B, *J. Geophys. Res.*, *103*(D24), 31,943–31,953, doi:10.1029/98JD01167.

Várnai, T., and A. Marshak (2002), Observations of three-dimensional radiative effects that influence MODIS cloud optical thickness retrievals, *J. Atmos. Sci.*, *59*(9), 1607–1618, doi:10.1175/1520-0469(2002)059<1607:OOTDRE>2.0.CO;2.

Waquet, F., J. Riedi, L. C. Labonnote, P. Goloub, B. Cairns, J.-L. Deuzé, and D. Tanré (2009), Aerosol remote sensing over clouds using A-Train observations, *J. Atmos. Sci.*, *66*, 2468–2480, doi:10.1175/2009JAS3026.1.

Wilcox, E. M. (2010), Stratocumulus cloud thickening beneath layers of absorbing smoke aerosol, *Atmos. Chem. Phys.*, *10*(23), 11,769–11,777, doi:10.5194/acp-10-11769-2010.

Wilcox, E. M. (2012), Direct and semi-direct radiative forcing of smoke aerosols over clouds, *Atmos. Chem. Phys.*, *12*(1), 139–149, doi:10.5194/acp-12-139-2012.

Wilcox, E. M., Harshvardhan, and S. Platnick (2009), Estimate of the impact of absorbing aerosol over cloud on the MODIS retrievals of cloud optical thickness and effective radius using two independent retrievals of liquid water path, *J. Geophys. Res.*, *114*, D05210, doi:10.1029/2008JD010589.

Wiscombe, W. (1980), Improved Mie scattering algorithms, *Appl. Optics*, *19*(9), 1505–1509.

Zhang, Z., K. Meyer, S. Platnick, L. Oreopoulos, D. Lee, and H. Yu (2014), A novel method for estimating shortwave direct radiative effect of above-cloud aerosols using CALIOP and MODIS data, *Atmos. Meas. Tech.*, *7*(6), 1777–1789, doi:10.5194/amt-7-1777-2014.